

## Article

# Expansion Pressure as a Probe for Mechanical Degradation in LiFePO<sub>4</sub> Prismatic Batteries

Shuaibang Liu <sup>1,2,†</sup>, Xue Li <sup>3,\*†</sup>, Jinhan Li <sup>1,2</sup>, Jintao Shi <sup>3</sup>, Xingcun Fan <sup>3</sup>, Zifeng Cong <sup>3</sup>, Xiaolong Feng <sup>3</sup>, Haoteng Li <sup>1,2</sup>, Wenwei Wang <sup>1,2,\*</sup>, Jiuchun Jiang <sup>1</sup>, Xiao-Guang Yang <sup>1,2,\*‡</sup>

<sup>1</sup> Shenzhen Automotive Research Institute, Beijing Institute of Technology, Shenzhen 518118, China; shuaibangliu@bit.edu.cn (S.L.); jiangjiuchun@szari.ac.cn (J.J.)

<sup>2</sup> National Engineering Research Center of Electric Vehicles, School of Mechanical Engineering, Beijing Institute of Technology, Beijing 100081, China

<sup>3</sup> China Automotive New Energy Technology Co., Ltd., Tianjin 300480, China

\* Correspondence: lixue@lishen.com.cn (X.L.); bitev@bit.edu.cn (W.W.); xgyang@bit.edu.cn (X.-G.Y.)

† These authors contributed equally to this work.

‡ Lead contact.

## Abstract

Battery mechanical properties degrade progressively with aging, manifesting as expansion pressure in module-constrained cells. Here, an in situ pressure operating system was developed to replicate the mechanical environment of lithium iron phosphate (LFP) prismatic batteries, enabling long-term monitoring under different loads and temperatures. Coupled with quasi-static compression tests on internal components, stress-strain curves and elasticity moduli were obtained to link microscopic behavior with macroscopic pressure response. Results show that irreversible pressure growth is jointly governed by state of health (SOH) and load: under low-load conditions, irreversible pressure increases non-linearly with SOH, whereas higher loads yield more linear trends. A multilevel physical model encompassing electrodes, cells, and modules was proposed to explain these behaviors. This model takes into account the influence of external pressure on the modulus of the battery, and indicates that SOH and load influence reversible pressure curves through their effect on modulus. A theoretical method was derived to calculate in-module modulus, confirming its linear correlation with the fluctuation amplitude of reversible pressure. Differential pressure-capacity analysis further demonstrated that characteristic changes in expansion pressure reflect modulus evolution, and deviations from this relationship reveal degradation pathways such as gas generation, solid electrolyte interphase (SEI) growth, or lithium plating. This study establishes pressure signals as mechanistic indicators of modulus evolution and provides a framework for diagnosing mechanical degradation in batteries.

Academic Editor: Odne S. Burheim

Received: 27 September 2025

Revised: 20 October 2025

Accepted: 22 October 2025

Published: 23 October 2025

**Citation:** Liu, S.; Li, X.; Li, J.; Shi, J.; Fan, X.; Cong, Z.; Feng, X.; Li, H.; Wang, W.; Jiang, J.; et al. Expansion Pressure as a Probe for Mechanical Degradation in LiFePO<sub>4</sub> Prismatic Batteries. *Batteries* **2025**, *11*, 391. <https://doi.org/10.3390/batteries11110391>

**Copyright:** © 2025 by the authors.

Licensee MDPI, Basel, Switzerland.

This article is an open access article distributed under the terms and conditions of the Creative Commons Attribution (CC BY) license (<https://creativecommons.org/licenses/by/4.0/>).

**Keywords:** prismatic battery; expansion pressure; mechanical degradation; elasticity modulus

## 1. Introduction

Lithium-ion batteries (LIBs) are central to the global transition toward renewable energy. Among various chemistries, LFP cathodes have gained wide adoption in electric vehicles (EVs) and electrochemical energy storage (EES) systems due to their safety and low cost [1]. In practical applications, cells are assembled into modules and packs, where

they are subjected to mechanical constraints [2,3]. These constraints, coupled with the inherent expansion of prismatic cells, generate internal pressures that can no longer be neglected. Expansion pressure directly affects both the safety [4] and performance [5] of LiBs, exerting a significant influence on their long-term reliability and service life [6]. Consequently, monitoring pressure evolution has emerged as a promising approach for estimating the state of charge (SOC) [7] and predicting the SOH [8,9] in next-generation battery management systems (BMS).

To mitigate the risks associated with uncontrolled deformation, a certain degree of compression is deliberately applied during cell stacking (Figure 1a). Such controlled loading helps stabilize internal interfaces and maintain electrochemical–mechanical integrity [10]. Moderate compression enhances interparticle contact [11], expels trapped gases [12,13], prevents electrode delamination [14], reduces gas generation [15], and slows capacity fade [16,17]. However, excessive loading introduces counterproductive effects: pore narrowing in electrodes and separators restricts ion transport, raises internal resistance, and accelerates parasitic reactions [18–21]. These dual effects highlight the delicate balance between beneficial and detrimental compression. For instance, Dobias et al. [22] reported that, within 15~75 kPa, higher pressure combined with low module stiffness slowed capacity fading in NMC622 pouch cells. In contrast, Aufschläger et al. [21] observed that compressing pouch cells from 75 to 1750 kPa increased anode pore resistance by 19%, with negligible changes in the cathode and separator. Jin et al. [23] further revealed that above 1000 kPa, graphite anode resistivity rises sharply, and under 3000 kPa, severe cycle fading occurs due to uneven SEI growth and lithium dendrite formation. These studies emphasize that compression, though necessary, must be carefully optimized.

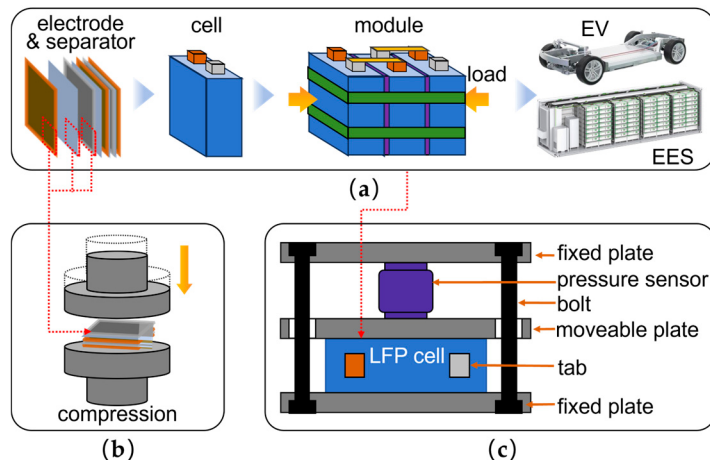


**Figure 1.** Illustration: (a) Hierarchical mechanical constraints diagram for battery application scenarios, from electrode sheet level to battery level, to module level, and finally to application level; (b) Quasi-static compression test to obtain stress–strain curves of electrode sheet, separator and full battery; (c) Experimental setup for simulating battery loading conditions and collecting expansion pressure, including fixed plates at both ends, movable plate in the middle, fastening bolts, LFP prismatic battery, and pressure sensor.

The mechanisms underlying pressure evolution can be traced to both electrochemical and mechanical origins. Specifically, expansion pressure results from the interplay between electrode volume changes during lithium intercalation/deintercalation and the effects of side reactions, all under external mechanical constraints [24]. This pressure can be divided into reversible and irreversible components. Reversible pressure arises from the

thermodynamic volume changes of active particles during lithiation/delithiation, manifesting as electrode thickness fluctuations [25–27]. Because these changes are directly linked to SOC, reversible pressure exhibits periodic variations and can serve as an additional indicator of battery state. For example, Mao et al. [7] incorporated pressure feedback into SOC estimation algorithms for LFP cells, improving accuracy in voltage plateau regions. In contrast, irreversible pressure originates from side reactions—such as SEI growth [28], electrolyte decomposition, gas evolution, and lithium plating [29,30]—that irreversibly increase internal volume [31]. This gradual accumulation of irreversible pressure correlates strongly with battery aging and SOH [32,33]. Notably, early-stage creep or densification under sustained compression may temporarily reduce irreversible pressure, although this effect diminishes with continued cycling [14]. These distinctions between reversible and irreversible contributions underscore why pressure analysis can reveal both instantaneous operating states and long-term degradation behaviors.

While the fundamental sources of pressure are understood, their actual evolution depends on multiple interrelated factors. Cannarella et al. [14] pioneered systematic investigations into reversible and irreversible pressure dynamics in pouch cells, showing that higher initial loads (0~1.5 MPa) amplified pressure fluctuations, accelerated irreversible pressure growth, and shortened cycle life. Li et al. [2] and Ding et al. [34] further demonstrated that irreversible pressure growth often precedes capacity fade, suggesting its utility as an early warning signal for catastrophic degradation. Moreover, distinct features in reversible pressure slopes have been linked to loss of lithium inventory (LLI), plating, or plastic deformation, while contraction of reversible pressure curves indicates loss of active material (LAM) [34]. Simulation studies reinforced these findings, showing that reversible pressure fluctuations scale directly with applied load [35]. Complementary mechanical tests by Wang et al. [36] revealed that as LFP prismatic cells age, their stress-strain curves shift rightward, modulus decreases, and reversible pressure fluctuations shrink under identical SOC and load. Together, these works suggest that pressure evolution captures both electrochemical and mechanical degradation signatures, though inconsistencies in methodology still limit comparability.

Despite these advances, critical knowledge gaps remain. Most prior studies emphasize either the pressure–SOC correlation or the pressure–SOH relationship, without fully accounting for the coupled mechanical-electrochemical system spanning electrodes, cells, and modules. Additionally, inconsistent units or test conditions hinder cross-study comparisons and have occasionally produced contradictory conclusions. In real-world modules, battery degradation encompasses not only electrochemical failure modes such as LLI and LAM but also evolving mechanical properties (e.g., modulus changes) driven by side reactions and sustained compression. Bridging these perspectives requires a standardized framework for analyzing expansion pressure and a reliable method for quantifying in-module modulus, thereby enabling more accurate interpretation of coupled degradation processes.

To address these challenges, this study develops an *in situ* pressure-operating system that replicates module-level mechanical environments. LFP prismatic cells are subjected to varied initial loads and temperatures, enabling systematic characterization of pressure evolution during cycling. Compression experiments on individual components provide stress–strain curves and compressive modulus values, clarifying how active expansion and passive compression jointly shape pressure dynamics. Building on these results, we propose a physical model that captures the multilevel, cross-scale mechanical system from electrode sheets to full modules. Our findings reveal that under low initial loads, reversible pressure fluctuations increase with irreversible pressure growth. Furthermore, we establish a theoretical framework for calculating in-module modulus and verify a linear correlation between modulus and reversible pressure fluctuation. Importantly, abnormal

modulus evolution is shown to reflect distinct mechanical degradation pathways. These insights not only deepen mechanistic understanding of electrochemical-mechanical coupling in LiBs but also provide a foundation for pressure-integrated BMS strategies that enhance both reliability and safety.

## 2. Materials and Methods

The batteries used in this study were commercial prismatic LFP cells with graphite anodes. Three cells were selected, and cyclic aging experiments were conducted under different combinations of temperature and initial load. To replicate the mechanical environment of cells within a module, each test battery was installed in a custom-designed pressure-measuring fixture (Figure 1c). In this setup, the fixed end plates were secured with bolts, constraining the battery uniaxially. As the battery expanded during cycling, the middle movable plate was displaced, transferring force to the load surface of the pressure sensor. The resulting expansion pressure was continuously monitored and recorded through the sensor's data acquisition system.

Guided by previous studies, the initial load range was targeted between 25 and 100 kPa. Considering both the safety limitations of prismatic cells and the irreversible pressure accumulation expected during long-term cycling, two representative initial loads—25 kPa and 50 kPa—were chosen. These values ensured experimental safety while maintaining the sensor response within the linear range of its rated capacity. Before commencing the cycling tests, the designated initial load was applied at 0% SOC and maintained for 48 h to allow for stress relaxation. During this preconditioning stage, the fastening bolts were fine-tuned iteratively to stabilize the pressure at the target load. The specific test configurations, including temperature and initial load for each cell, are summarized in Table 1. Choosing different temperatures causes the aging speed of the battery to change through temperature, so as to obtain a battery with different aging degrees and its pressure data within the same time period, and at the same time observe the influence of temperature on pressure. For the specific numerical values of the settings, please refer to Appendix A.

**Table 1.** Experimental condition setup.

Sample Number	Temperature	Initial Load
#1	25 °C	50 kPa
#2	45 °C	50 kPa
#3	55 °C	25 kPa

Long-term cycling tests were performed in thermostatic chambers at the specified temperatures. The cycling and reference performance test (RPT) procedures are summarized in Table 2. The cycling protocol (steps 1~5) consisted of constant-current charging to 3.8 V at 1.6C-MCC (a Multi-stage Constant Current protocol was adopted to simulate the fast charging process of the battery; the specific MCC charging procedures can be found in Appendix A), followed by constant-voltage charging until the current decreased below C/20, a 1800 s rest, constant-current discharging to 2.0 V at 1C (discharge the battery at the normal rate), and a final 1800 s rest. To track degradation, RPTs (steps 6~9) were conducted every 100 cycles, during which charging and discharging were performed at C/3 (regular small-rate detection of the battery during actual usage). Before each RPT, the thermostat was adjusted to 25 °C and maintained for 8 h to ensure thermal stabilization. After the RPT, the chamber temperature was restored to the designated cycling temperature, and another 8 h rest was applied before cycling resumed. Throughout the entire test, pressure sensor signals were recorded in real time and converted into expansion pressure with a sampling frequency of 1 Hz.

**Table 2.** Test step setup.

Step	Operation
1	Charge at 1.6C-MCC to 3.8 V, CV to C/20
2	Rest for 1800 s
3	Discharge at 1C-CC to 2 V
4	Rest for 1800 s
5	Cycle steps 1 to 4 for 100 cycles
6	Charge at C/3-CC to 3.8 V, CV to C/20
7	Rest for 1800 s
8	Discharge at C/3-CC to 2 V
9	Rest for 1800 s
10	Cycle steps 1 to 9

Since the modulus of batteries cannot be measured directly, quasi-static compression experiments were also performed on components extracted from fresh LFP batteries to investigate their mechanical characteristics and simulate the squeezing process in modules (Figure 1b). Stress–strain curves were collected for positive electrode sheets, negative electrode sheets, separators, dry cells (pouch cells without electrolyte), and wet cells (pouch cells with electrolyte), enabling analysis of both individual components and their combined behaviors under compression. Each component was cut into smaller pieces and stacked to match the dimensions of the compression platform. To maintain structural integrity, stacked positive and negative electrode sheets were wrapped with separators to prevent tearing and active material detachment, while separators were folded in a zigzag pattern. Dry and wet cells were prepared following the standard laminated battery manufacturing process and vacuum-sealed in aluminum-plastic films, with electrolyte injected only into the wet cells. This design enabled direct comparison of the influence of electrolyte on compression characteristics. Details of sample preparation and corresponding photographs are provided in Appendix B.

### 3. Results and Discussion

#### 3.1. Lifespan Decline and Compression Effects Jointly Drive Irreversible Pressure Growth

The discharge pressure profiles obtained from the RPTs at 25 °C–50 kPa, 45 °C–50 kPa, and 55 °C–25 kPa are shown in Figure 2a–c. The x-axis represents normalized discharge capacity, while the y-axis denotes pressure. To enable direct comparison of curve morphology among different cells, the ordinate scale and intervals were kept identical across all three figures. It should be noted that pressure data for the 100th cycle of the 25 °C–50 kPa sample and the 300th cycle of the 45 °C–50 kPa sample were not fully recorded due to operational issues and are therefore excluded.

All three samples exhibit a progressive upward shift in the pressure curves with cycling, consistent with the widely reported phenomenon of irreversible pressure growth. The 25 °C–50 kPa sample shows relatively closely spaced curves, whereas the 45 °C–50 kPa sample exhibits wider spacing, indicating that higher temperatures accelerate irreversible pressure accumulation. For the 55 °C–25 kPa sample, curve spacing increases gradually with cycle number: the curves are relatively flat at early stages but become progressively steeper as irreversible pressure builds, eventually approaching the shapes observed for the 25 °C–50 kPa and 45 °C–50 kPa samples. This staged evolution is less apparent in the higher-load samples, suggesting that reversible pressure contributions grow with applied load.

The observed variation in pressure-capacity behavior, driven by modulus evolution, differs from previous findings on pouch cells, which typically exhibit a monotonically increasing modulus [34]. In prismatic batteries, a lower applied load corresponds to a lower modulus [37]. Under such conditions, active material expansion more readily deforms the cell under external constraints, compressing the internal structure. With increasing external load, internal densification raises the modulus, amplifying the extent to which active material expansion translates into external pressure. Consequently, applied load enhances the reversible pressure response. A more detailed analysis of this mechanism is provided in Section 3.2.

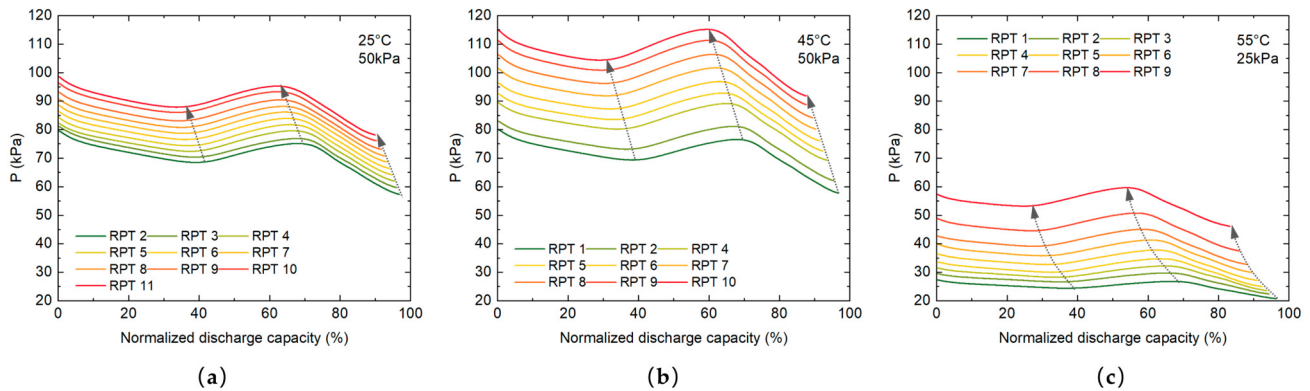


**Figure 2.** Expansion pressure profiles during the RPT discharge process: (a)  $25^{\circ}\text{C}$ – $50\text{kPa}$ ; (b)  $45^{\circ}\text{C}$ – $50\text{kPa}$ ; (c)  $55^{\circ}\text{C}$ – $25\text{kPa}$ . Gray arrows indicate the direction of inflection point shifts.

To investigate the evolution of this phenomenon during battery cycling, the discharge capacity of each battery during the RPTs was extracted. The  $SOH$  was defined as the normalized discharge capacity, as expressed in Equation (1):

$$SOH = \frac{Q}{Q_0} \times 100\% \quad (1)$$

where  $Q$  is the current discharge capacity and  $Q_0$  is the discharge capacity of the first cycle.

The  $SOH$  decay curves of the three samples are shown in Figure 3a. The cells exhibit distinct degradation rates at different temperatures, with an overall trend of faster decay at higher temperatures. Both the  $25^{\circ}\text{C}$ - $50\text{kPa}$  and  $45^{\circ}\text{C}$ - $50\text{kPa}$  samples display two-stage behavior. During the first 100 cycles, capacity declines rapidly, primarily due to extensive SEI formation at beginning of life (BOL), which consumes active lithium and electrolyte [38]. After this initial stage,  $SOH$  decreases linearly with cycling. The decay rate is higher at  $45^{\circ}\text{C}$ , attributed to accelerated SEI formation and the repeated cracking-regeneration process at elevated temperatures, which accelerate lithium inventory loss [28,39].

In contrast, the  $55^{\circ}\text{C}$ - $25\text{kPa}$  sample shows a more complex, four-stage degradation process. The first stage (0~100 cycles) mirrors the initial decay observed in the other two samples. The second stage (100~300 cycles) exhibits a slower linear decay, comparable to the  $45^{\circ}\text{C}$ - $50\text{kPa}$  cell, suggesting that the lower load mitigates high-temperature effects. This mitigation may arise from the lower modulus [35] and higher porosity [11] under reduced compression, which suppress local side reactions. For instance, Cannarella et al. [18] reported that higher local loads reduce porosity, increase impedance, and degrade performance. In the third stage (300~700 cycles), capacity loss accelerates but remains largely linear. Finally, after 700 cycles,  $SOH$  declines nonlinearly, likely due to cumulative porosity loss from SEI thickening and irreversible pressure buildup, which intensifies side reactions such as lithium plating, or reduces active material utilization through electrolyte depletion.

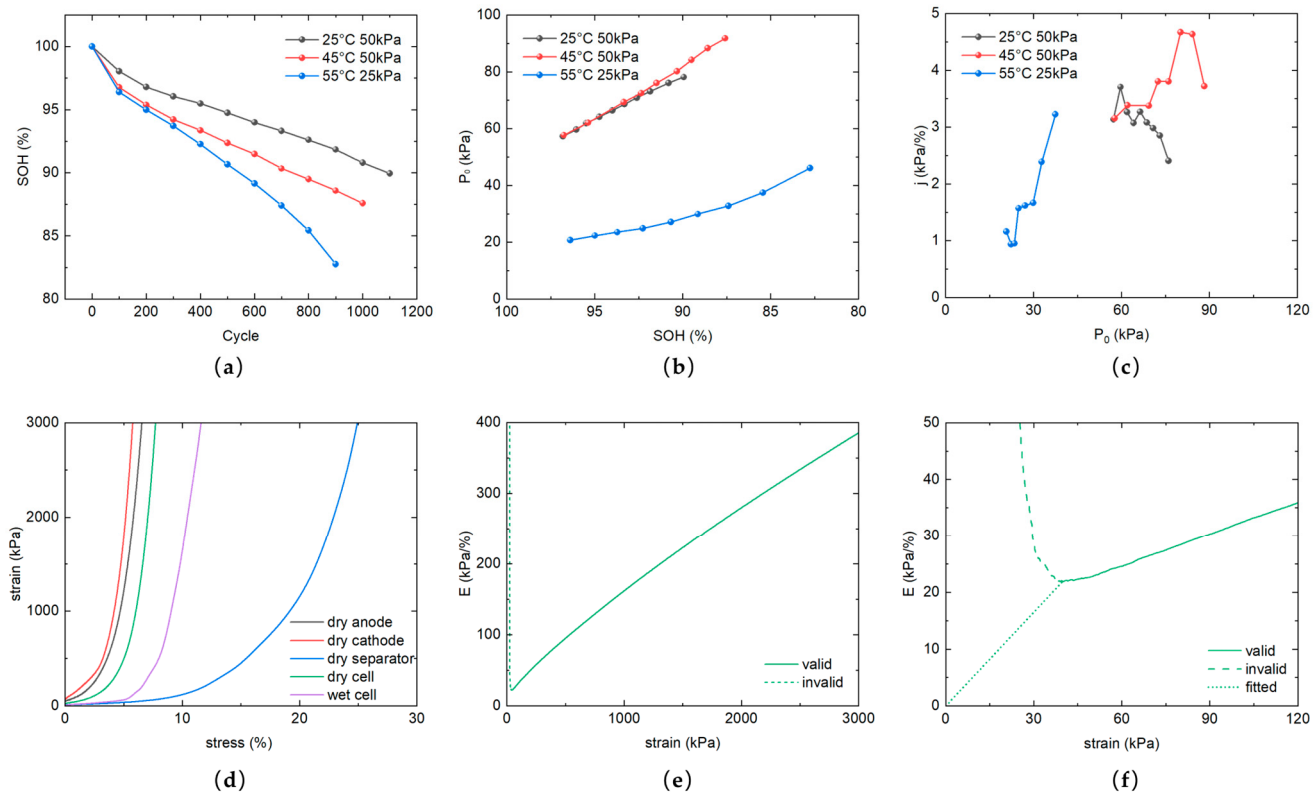


**Figure 3.** Irreversible pressure evolution of LFP cells under different conditions: (a) SOH as a function of cycle number; (b) irreversible pressure  $P_0$  versus SOH; (c) slope  $j$  as a function of  $P_0$ ; (d) stress–strain curves of electrodes, separator, dry cell, and wet cell; (e) evolution of cell elastic modulus with pressure; (f) magnified view of the 0–120 kPa modulus curve with fitted segment.

The irreversible pressure,  $P_0$ , defined as the cell pressure at 0% SOC, is plotted as a function of SOH in Figure 3b. For the 55 °C-25 kPa sample,  $P_0$  decreases initially, likely because (1) stress relaxation is a prolonged process, and the 48 h preconditioning period was insufficient for stabilization, and (2) relaxation proceeds more slowly under lower applied loads. During subsequent cycling, the 25 °C-50 kPa and 45 °C-50 kPa samples show nearly identical linear trends (this means that compared with thermal expansion, the pressure increase caused by electrochemical side reactions has a greater impact; for detailed analysis, please refer to Appendix C), both with steeper slopes than the 55 °C-25 kPa sample, while the latter displays nonlinear behavior.

To quantify this, the incremental slope  $j$  between adjacent data points was defined as:

$$j = \frac{P_{0(i+1)} - P_{0(i)}}{SOH_{(i)} - SOH_{(i+1)}} \quad (2)$$

where  $P_{0(i)}$  and  $SOH_{(i)}$  represent the irreversible pressure and SOH at the current point, and  $P_{0(i+1)}$  and  $SOH_{(i+1)}$  represent those at the next point. Physically,  $j$  represents the increase in irreversible pressure per unit loss of SOH, which means that constant  $j$  suggests  $\Delta P$  is linearly proportional to  $\Delta SOH$ . As shown in Figure 3c,  $j$  remains nearly constant under higher loads but increases with  $P_0$  under lower load, indicating that irreversible pressure correlates linearly with SOH only under high-load conditions. Thus, the coupling effect of load must be considered when applying irreversible pressure as an SOH diagnostic.

To further elucidate these results, stress–strain curves of individual components and composite cells were measured (Figure 3d). At low loads, all samples exhibit flat curves

that steepen with increasing compression. Among individual components, the separator shows the highest modulus, while the positive electrode exhibits the smallest strain, followed by the negative electrode. Wet cells deform more than dry cells, and their stress-strain curves lie between those of the separator and electrodes. The primary difference is a delayed inflection point in the wet cell curve, attributable to creep in the electrolyte-infiltrated multilayer structure, which requires a longer compression stroke to stabilize. Because long-term resting in this study eliminated creep in the main battery tests, the dry-cell stress-strain curve was selected to represent the *in situ* mechanical properties of the cells.

According to the definition of elasticity modulus (3):

$$E = \frac{\sigma}{\epsilon} \quad (3)$$

where  $E$  is the elasticity modulus,  $\sigma$  is stress, and  $\epsilon$  is strain.

The modulus curve of the cell is presented in Figure 3e, where the solid line represents valid data and the short dashed line corresponds to missing strain information during initial loading due to operational limitations. The results show that the battery modulus gradually increases with compression, consistent with literature reports [35–37,40]. The 0–120 kPa segment of the curve in Figure 3e is enlarged in Figure 3f. From the perspective of material mechanics, the stress-strain curve in the dashed interval should originate from the origin and smoothly connect with the solid line. Accordingly, a dotted line was used to fit this segment, revealing that the growth rate of  $E$  with strain in this region is relatively steep.

This trend is consistent with the behavior observed in Figure 3c. Together, the two sets of results indicate the following relationship: for the low-load sample (55 °C–25 kPa), irreversible pressure increases progressively during cycling, leading to a rise in modulus. As irreversible pressure accumulates, the rate of modulus growth declines, while the rate of irreversible pressure growth gradually converges toward that of the high-load samples (25 °C–50 kPa and 45 °C–50 kPa). At the same time, the amplitude of reversible pressure fluctuations also approaches that of the higher-load samples.

### 3.2. The Coupled Effects of Load and Aging on Reversible Pressure

The intrinsic mechanism of volume expansion in LFP cells arises from the strain of active materials in the positive and negative electrodes during lithium intercalation and deintercalation. Prior studies have shown that the graphite anode undergoes a three-stage nonlinear volume change [41]. In particular, when the stoichiometric number lies between 0.6 and 0.3—corresponding to the stage II → stage III transition (Figure 4c)—the unit lattice volume remains nearly unchanged. In this regime, lithium ions are rearranged within the existing graphite layers rather than occupying new layers, causing negligible changes in interlayer spacing and resulting in a markedly reduced rate of particle volume change.

By contrast, the volume change of the LFP cathode during lithium intercalation and deintercalation follows an approximately linear trend [41,42]. Under the combined effect of both electrodes, the nonlinear behavior of graphite strongly influences the full-cell pressure response, especially the position of curve inflection points. As shown in Figure 4b, the free-state deformation of the electrodes demonstrates that during the stage II → stage III transition, the negative electrode volume change rate drops significantly below that of the positive electrode [42]. Consequently, the cathode temporarily dominates the cell's deformation behavior, leading to a reversal in the direction of pressure evolution in the full LFP cell (Figure 4a).

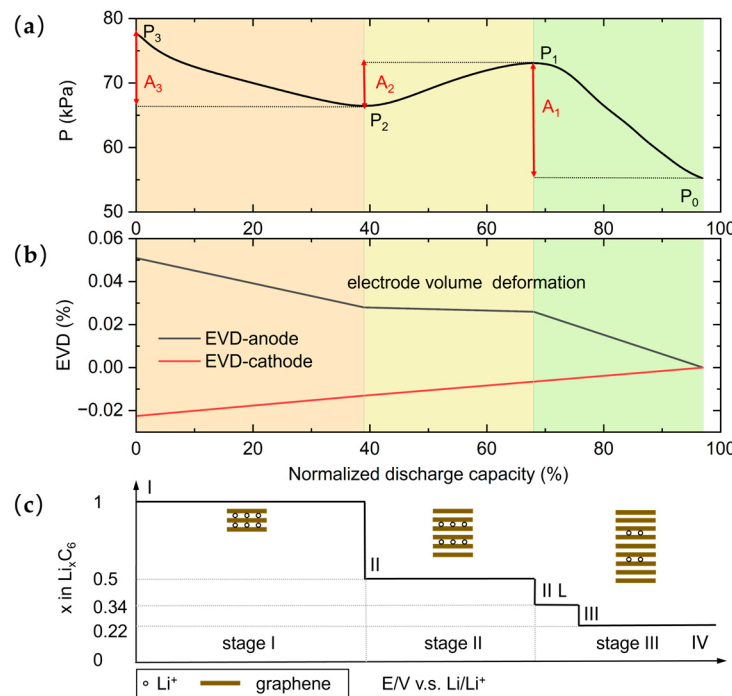


**Figure 4.** Pressure and electrode volume evolution during battery discharge: (a) Pressure curve and definition of characteristic points (example shown from the 200th cycle at 25 °C-50 kPa); (b) Free-state volume deformation curves of LFP cathode and graphite anode (data adapted from Ref. [42], corrected based on the inflection point in panel A); (c) Stage formation process during lithium-ion intercalation into graphite (data from Ref. [43]).

The expansion pressure of a battery arises from the combined effects of electrode sheet volume deformation during charge–discharge cycling, the multilayer elastic structure inside the cell, and external mechanical constraints. In practice, electrode deformation under load may deviate from the free-state (the mechanical state of the cell without external compression) behavior shown in Figure 4b, and by-products of side reactions can further alter the mechanical properties of the internal multilayer structure. As a result, the shape of the reversible pressure curve evolves with both  $P_0$  and SOH.

To investigate these effects, the reversible pressure curve was divided into three segments corresponding to the three graphite volume-change stages (Figure 4c), as illustrated in Figure 4a. Taking the 200th-cycle reversible pressure curve of the 25 °C–50 kPa sample as an example,  $P_1$  and  $P_2$  are defined as the transition points between stage III → II and stage II → I, respectively.  $P_3$  corresponds to the initial discharge point, which is also the maximum of the discharge expansion pressure curve. The vertical spans of each stage are denoted as  $A_1$ ,  $A_2$ , and  $A_3$ , representing the fluctuation amplitudes of reversible pressure in stages III, II, and I, respectively. Their relative variations during aging ( $\Delta A_1$ ,  $\Delta A_2$ ,  $\Delta A_3$ ) were evaluated against both SOH and  $P_0$ . Figure 5a–c presents the evolution of  $\Delta A_1$ ,  $\Delta A_2$ , and  $\Delta A_3$  with SOH, while Figure 5d–f shows their dependence on  $P_0$ . Here,  $\Delta A_1$  is defined as the change in  $A_1$  relative to its initial value, with  $\Delta A_2$  and  $\Delta A_3$  defined analogously.

For the 25 °C–50 kPa and 45 °C–50 kPa samples, both  $\Delta A_1$  and  $\Delta A_2$  increase with aging. This is because the irreversible pressure increases during aging, leading to an increase in modulus. At elevated temperatures, growth becomes more pronounced—this phenomenon is ascribed to intensified reversible pressure fluctuations caused by thermal expansion. In the 55 °C–25 kPa sample, the increase in reversible pressure fluctuation arises not only from thermal expansion but also from nonlinear growth of modulus. However, this effect diminishes as irreversible pressure  $P_0$  accumulates, as shown in Figure 5d,f. The evolution of  $\Delta A_3$  differs from that of  $\Delta A_1$  and  $\Delta A_2$ . For the 25 °C–50 kPa and 45 °C–50 kPa

samples,  $\Delta A_3$  first decreases and then increases with declining SOH (Figure 5c). The initial decrease is caused by the shortening of stage I, which reduces  $A_3$  (Figure 6b). At later stages, increasing  $P_0$  enhances the battery modulus, driving a gradual recovery of  $A_3$ .

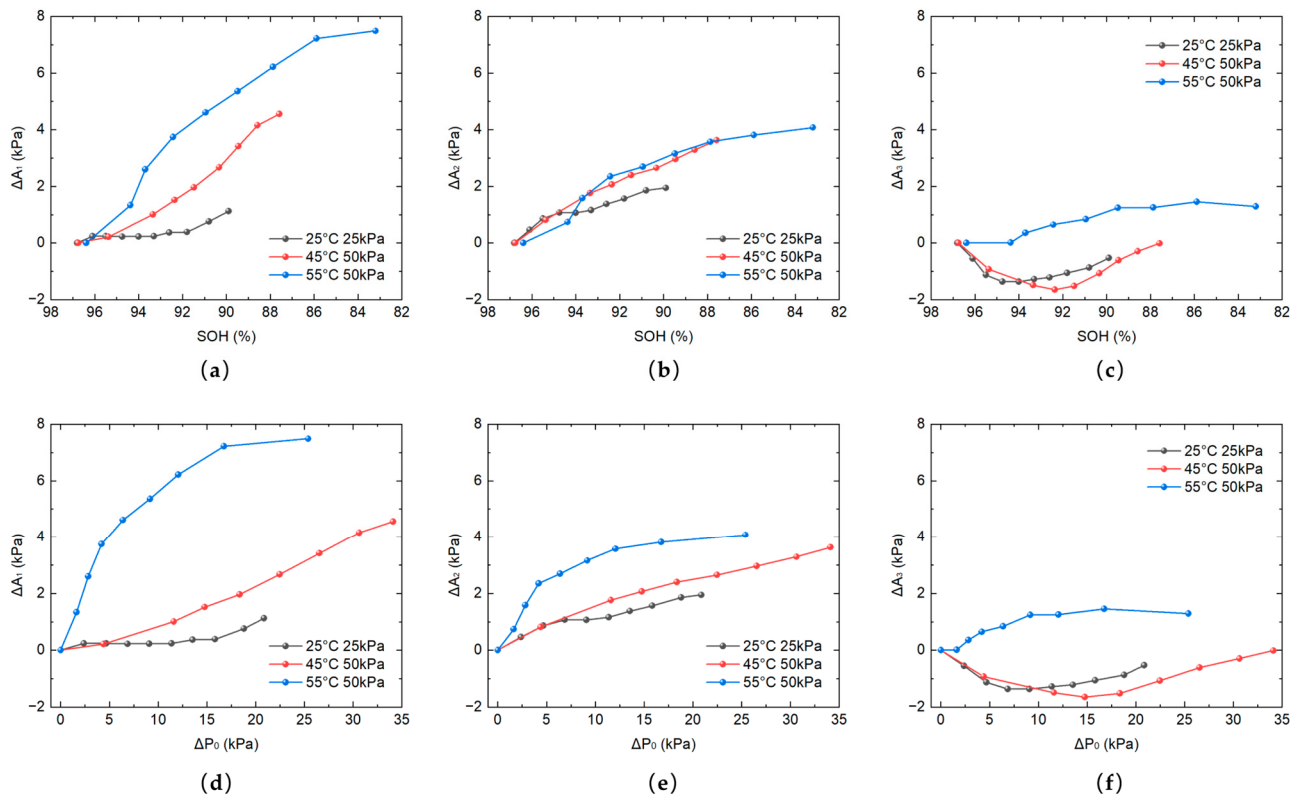


**Figure 5.** Evolution of vertical pressure characteristics as a function of SOH and irreversible pressure  $P_0$ : (a)  $\Delta A_1$  vs. SOH; (b)  $\Delta A_2$  vs. SOH; (c)  $\Delta A_3$  vs. SOH; (d)  $\Delta A_1$  vs.  $\Delta P_0$ ; (e)  $\Delta A_2$  vs.  $\Delta P_0$ ; (f)  $\Delta A_3$  vs.  $\Delta P_0$ .

In summary, these results demonstrate that reversible pressure evolution is jointly governed by electrode phase transitions, thermal effects, and modulus changes induced by both load and aging, underscoring the strong coupling between electrochemical and mechanical degradation mechanisms.

To further interpret the phenomena described above, a physical model of a multi-level, cross-scale mechanical system—spanning electrode sheets, cells, and modules—was established, as illustrated in Figure 6a. This model captures the evolution of expansion pressure across the full battery lifecycle, including the free state, initial loading, discharge, cyclic aging, and post-aging charge. A detailed analysis of the model is presented below.

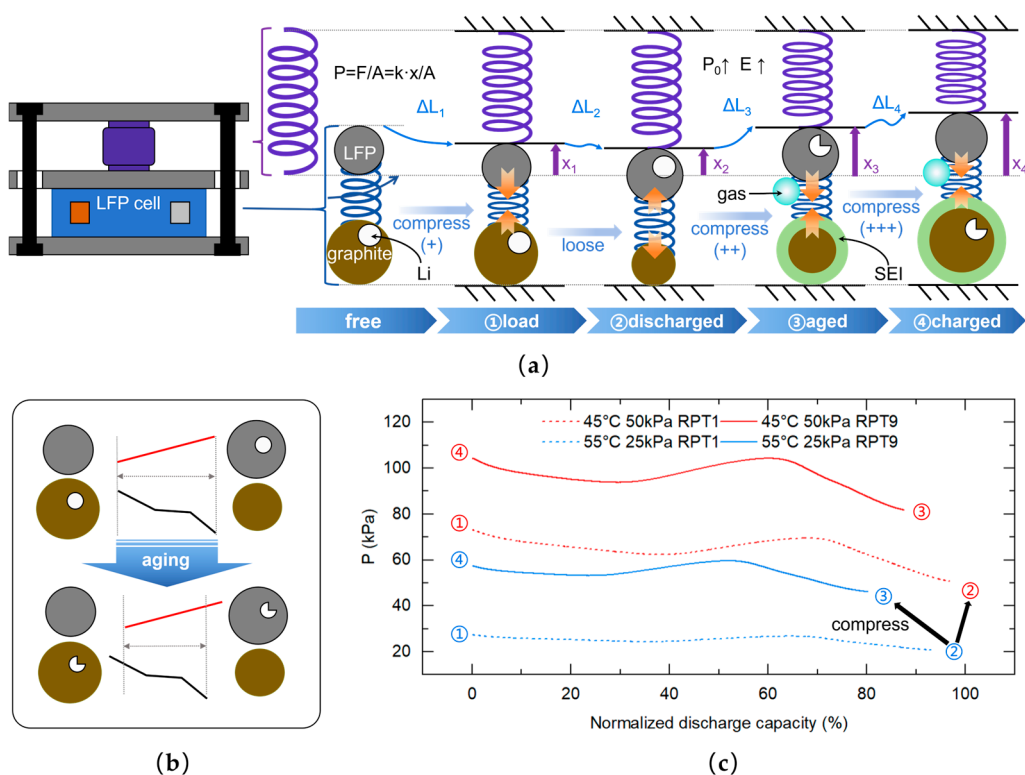


**Figure 6.** Schematic diagram of the physical model of the multi-level cross-scale mechanical system of electrode sheets-battery-module: (a) Mechanical responses of LFP batteries and pressure sensors under different states; (b) Changes in the volume expansion curves of the cathode and anode electrodes when lithium inventory is lost; (c) Comparison of pressure curves of fresh batteries and aged batteries under different loads.

First, the pressure sensor operates consistently within its linear working range and can therefore be modeled as a linear spring. The output of the expansion pressure follows Hooke's law, expressed in Equation (4):

$$P = \frac{F}{A} = \frac{kx}{A} \quad (4)$$

where  $P$  is the battery expansion pressure,  $F$  is the force exerted on the battery (equal to the sensor force),  $A$  is the load-bearing area of the battery,  $k$  is the linear stiffness of the sensor, and  $x$  is the displacement of the sensor's load surface. In Figure 6a, the thick purple arrow represents the displacement direction, with the dashed line indicating the initial sensor position.

LiBs, in contrast, are porous multilayer viscoelastic bodies comprising solid–liquid mixtures, whose mechanical properties can be approximated by a spring-damper model. Since the batteries in this study experienced sufficient stress relaxation at BOL, and given the low C-rates and slow volumetric changes during cycling (quasi-static loading), damping effects can be neglected. Thus, the battery is modeled as a nonlinear spring (Figure 6a, “free” state). This choice reflects the nonlinear evolution of modulus during loading. In the schematic, gray circles denote LFP cathode particles, brown circles denote graphite anode particles, white circles represent intercalated lithium, white sectors indicate consumed lithium inventory, green rings mark SEI films on graphite surfaces, and blue-highlighted circles represent gases generated by side reactions.

In Figure 6a,  $\Delta L$  denotes the relative thickness change of the battery between successive states, with blue arrows showing pressure trends. The mechanical evolution process is explained below using the 55 °C–25 kPa sample as an example:

① Load: When the battery and sensor are clamped in the fixture, both deform under the initial load. The porous multilayer structure of the battery is compressed from the free state, as indicated by the orange arrow in Figure 6a, with a deformation of  $\Delta L_1$ . The relationship between  $\Delta L_1$  and load depends on the nonlinear modulus. At this stage, the sensor displacement is  $x_1$ .

② Discharge: During discharge, the shrinkage of the graphite anode exceeds the expansion of the LFP cathode, reducing the overall battery thickness by  $\Delta L_2$ . The sensor displacement decreases to  $x_2$ , the expansion pressure falls, and the porous structure partially relaxes.

③ Aged: With continued cycling, side reactions consume electrolyte and form SEI and gases, as exemplified by Equation (5) [44]:



Electrolyte loss reduces internal buffering, while SEI and gas accumulation enlarge the battery volume and pressure [3,28], driving growth of irreversible pressure  $P_0$ . Consequently, sensor compression increases to  $x_3$ , and elevated pressure further densifies the battery, increasing its modulus  $E$ . This complements findings by Wang et al. [36], who observed modulus decreases in aged free-state cells. The thickness increment  $\Delta L_3$  corresponds to the  $P_0$ -SOH trajectory of the 55 °C–25 kPa sample (Figure 3b) and follows Equation (6):

$$\Delta L_3 = \frac{\Delta P_0 A}{k} \quad (6)$$

Indicating that irreversible pressure growth is proportional to thickness increase.

④ Charge: After aging, the reduced buffering capacity means particle expansion contributes more directly to battery thickening rather than compressing internal space. Hence,  $\Delta L_4$  in the 55 °C–25 kPa sample exceeds  $\Delta L_2$ , and reversible pressure fluctuations intensify with increasing  $P_0$ . At this stage, sensor compression reaches  $x_4$ , with  $(x_4 - x_3) > (x_2 - x_1)$ . Under higher loads, however,  $\Delta L_4$  is not necessarily greater than  $\Delta L_2$ , because lithium inventory loss shortens stage I, reducing  $A_3$ . For example, in the 45 °C–50 kPa sample, the initially higher  $P_0$  (Figure 5c, black arrow) places the battery beyond the nonlinear growth regime, leading to a more linear  $P_0$ -SOH relationship during cycling (Figure 3b).

### 3.3. Quantitative Analysis of the Battery Elastic Modulus

Building on the preceding analysis, we now aim to identify quantitative indicators of modulus from the expansion pressure curve. Typically, pores in battery electrode sheets and separators are uniformly distributed, with porosity values around 0.3 [5,45]. Because electrode sheets constitute the majority of the battery volume, the overall battery porosity can be approximated as equivalent to that of the electrodes. The relationship between modulus and porosity is generally a negative linear correlation [46], described in Equation (7):

$$E = E_0(1 - \alpha p) \quad (7)$$

where  $E$  is the battery modulus,  $E_0$  is the modulus at zero porosity,  $\alpha$  is a correlation constant, and  $p$  is the porosity.

Previous studies have shown that electrode sheet expansion arises from a combination of porosity and the partial molar volume of active materials, manifesting as thickness changes at the electrode scale [26]. Thus, the electrode sheet thickness increment can be expressed as Equation (8):

$$\frac{\Delta L}{L_0} = \varepsilon_s \frac{\Delta V}{V_0} \quad (8)$$

where  $\Delta L$  is the thickness increment of the positive electrode sheet,  $L_0$  is its original thickness,  $\varepsilon_s$  is the solid-phase volume fraction,  $\Delta V$  is the volume increase of LFP particles, and  $V_0$  is the original particle volume. Since LFP particles expand linearly,  $\Delta V/V_0$  may be treated as a constant.

The solid-phase fraction and porosity are approximately complementary, as expressed in Equation (9):

$$\varepsilon_s = 1 - p \quad (9)$$

Because expansion in stages I and III is influenced by both electrodes, while graphite volume remains essentially unchanged in stage II, the expansion pressure curve in stage II reflects primarily the positive electrode. Under low-rate conditions, the full-cell thickness change in stage II is therefore driven by LFP expansion. The thickness increment of the positive electrode in stage II can be written as Equation (10):

$$\frac{\Delta L}{L_0} = \frac{\Delta x_{stageII}}{\Delta Q_{N,stageII} 2nL_0} \quad (10)$$

where  $\Delta x_{stageII}$  is the thickness change in stage II,  $\Delta Q_{N,stageII}$  is the normalized capacity in stage II,  $n$  is the number of positive electrode sheets, and the factor 2 accounts for double-sided coating.

According to the physical model of the electrode sheet-battery-module multiscale system,  $\Delta x_{stageII}$  can be expressed in terms of expansion pressure via Equation (4), yielding Equation (11):

$$\Delta x_{stageII} = \frac{\Delta P_{stageII} A}{k} \quad (11)$$

Based on Equations (8) and (9), the thickness increment can be further expressed as:

$$\frac{\Delta L}{L_0} = \frac{\Delta P_{stageII} A}{\Delta Q_{N,stageII} 2nL_0 k} \quad (12)$$

To minimize inconsistencies caused by pressure variations within stage II and transition effects near inflection points (arising from graphite volume changes and internal heterogeneity), Equation (12) is reformulated in differential form. The maximum differential value is taken, as shown in Equation (13):

$$\frac{\Delta L}{L_0} = \frac{A}{2nL_0 k} \left( \frac{dP}{dQ_N} \right)_{max,stageII} \quad (13)$$

Finally, by combining Equations (7)–(9) and (13), the expression for modulus is obtained as Equation (14):

$$E = E_0 \alpha \frac{V_0}{\Delta V} \frac{A}{2nL_0 k} \left( \frac{dP}{dQ_N} \right)_{max,stageII} + E_0 (1 - \alpha) \quad (14)$$

In Equation (14), all parameters except  $P$  and  $Q_N$  are constants. Thus, the modulus is linearly and positively correlated with the maximum value of  $dP/dQ_N$  in the stage II segment ( $(dP/dQ_N)_{max, stageII}$ ). In practice, the evolution of battery modulus can be quantified by

differentiating the  $P$ - $Q_N$  curve and extracting the maximum value within stage II. The differential curves ( $dP/dQ_N$ ) of the three samples are plotted in Figure 7a–c. Detailed information on the curve processing method and corresponding pictures are provided in Appendix D.

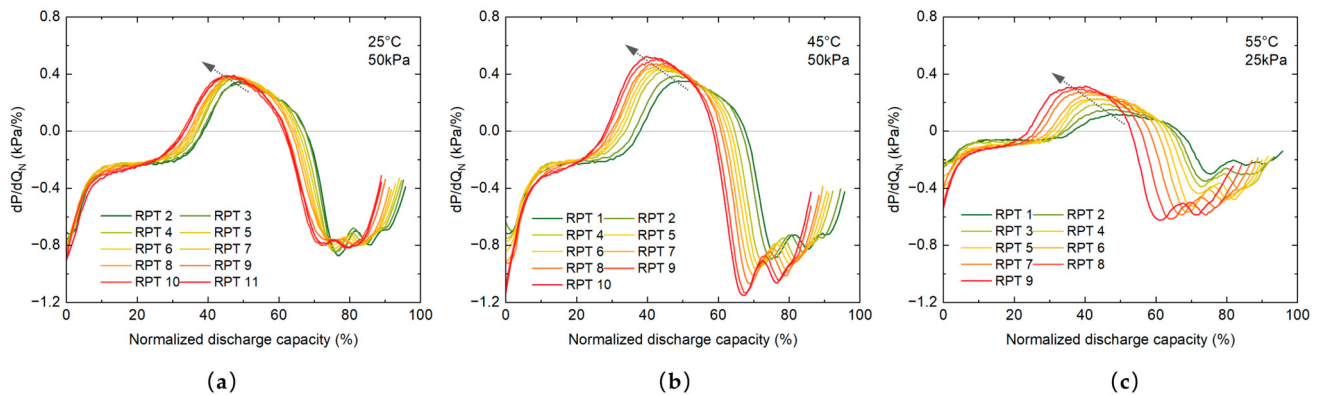


**Figure 7.** Differential pressure-capacity ( $dP/dQ_N$  vs.  $Q_N$ ) curves: for (a) 25 °C–50 kPa, (b) 45 °C–50 kPa, and (c) 55 °C–25 kPa. Gray arrows indicate the movement direction of the stage II vertex.

As indicated in the figures, the  $(dP/dQ_N)_{\max, \text{stage II}}$  values of all three samples increase progressively with aging (gray arrows). The  $(dP/dQ_N)_{\max, \text{stage II}}$  of the low-load sample (55 °C–25 kPa) remains significantly smaller than those of the two high-load samples, and the modulus follows the same trend as  $(dP/dQ_N)_{\max, \text{stage II}}$ , thereby validating the preceding discussion of Equations (7)–(14). In the  $dP/dQ_N$  curve of the fresh battery (green trace), three distinct valleys appear in the stage III region. The  $(dP/dQ_N)_{\max, \text{stage II}}$  reflects the actual expansion rate of the battery under compression conditions. The greater the actual expansion rate, the more difficult the battery is to be compressed, which indicates a larger modulus. We also noticed that the rightmost valley gradually vanishes with aging, likely due to enhanced internal heterogeneity within the battery. This feature can therefore serve as a potential indicator of aging.

To further quantify this relationship, the  $(dP/dQ_N)_{\max, \text{stage II}}$  values of all three samples were extracted and plotted in Figure 8a, where the ordinate corresponds to the right axis and the abscissa represents the pressure associated with  $(dP/dQ_N)_{\max, \text{stage II}}$ . For comparison, the E-strain curve is plotted with the same abscissa but a separate ordinate scale, enabling direct comparison between  $E$  and  $(dP/dQ_N)_{\max, \text{stage II}}$ . In the low-load regime, the  $(dP/dQ_N)_{\max, \text{stage II}}$ –strain relationship shows excellent agreement with the E-strain curve, further confirming the linear positive correlation between  $E$  and  $(dP/dQ_N)_{\max, \text{stage II}}$ . Based on the proportional relationship in Figure 8, the approximate quantitative relationship between  $E$  and  $(dP/dQ_N)_{\max, \text{stage II}}$  is expressed in Equation (15):

$$E = 50 \frac{dP}{dQ_N} + 7.25 \quad (15)$$

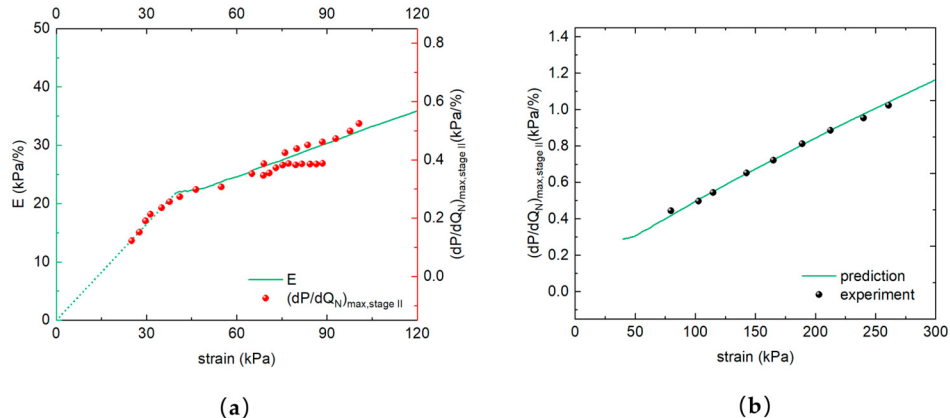


**Figure 8.** The fitting process of the model and its predictive capability: (a) The relationship between  $(dP/dQ_N)_{\text{max, stage II}}$  (in red) and  $E$  (in green) and pressure/strain; (b) Comparison between the experimental results and the predicted results.

The adaptability of this physical relationship is limited by the specifications of the module and the battery. According to Equation (14), the variables that affect this relationship include the module stiffness  $k$ , the battery area  $A$ , the initial thickness of the electrode sheet  $L_0$ , the number of positive layers  $n$ , and the intrinsic relationship between the modulus and porosity. For batteries and modules of uniform specifications, this physical relationship is adaptable.

If  $E$  is written on the right side of the equation, then Equation (15) can be expressed as Equation (16):

$$\left( \frac{dP}{dQ_N} \right)_{\text{max, stage II}} = \frac{E}{50} - \frac{29}{200} \quad (16)$$

When the elastic modulus  $E$  of the battery is known, Equation (16) can be used to predict the behavior of the battery pressure curve. We set up a group of accelerated aging experiments to verify the effectiveness of this model. The temperature during the experiment was set at 60 °C, and the initial load was 50 kPa (the RPT pressure data of the verification experiment is detailed in Appendix E). The comparison of the experimental and predicted results is shown in Figure 8b, and the two show a high degree of coincidence. It can be seen that the model we proposed can accurately capture the pressure behavior of the battery and its evolution trend. Compared with other existing models in the literature, the advantage of this model lies in establishing a connection between the evolution of pressure behavior and the constitutive mechanical characteristics of the battery, revealing the reasons for the irreversible change in pressure characteristics, and predicting the long-term pressure evolution trend of the battery with a small amount of experimental data.

When the evolution of  $(dP/dQ_N)_{\text{max, stage II}}$  with strain deviates from the expected  $E$ -strain curve, it suggests that factors beyond porosity changes are influencing the battery modulus. Such factors include abnormal gas generation, excessive SEI growth, or irreversible lithium plating. Abnormal gas generation and the accumulation of low-modulus SEI components can reduce the overall modulus of the battery [34], whereas irreversible lithium plating increases modulus by introducing rigid metallic deposits. The framework proposed in this study therefore provides a mechanistic basis for diagnosing these degradation failure modes.

#### 4. Conclusions

This study systematically investigated the evolution of expansion pressure in prismatic LFP batteries and revealed that both irreversible and reversible pressure components are governed by the coupling of SOH and external load. We showed that irreversible pressure growth is strongly influenced by changes in battery modulus, which itself evolves with load and aging. A multiscale physical model was established to interpret these effects, demonstrating that under low-load conditions, batteries exhibit low modulus, so the same active material expansion results in greater internal compression but smaller external thickness change. By contrast, as load increases or aging progresses, irreversible pressure accumulates, the porous internal structure densifies, modulus rises, and external thickness change becomes larger. This explains why stage-specific amplitudes ( $A_1$  and  $A_2$ ) increase steadily with cycling, while  $A_3$  first decreases due to the shortening of stage I and then recovers as modulus growth dominates. Quantitative analysis further revealed that the maximum slope of the stage II segment in the pressure-capacity differential curve,  $(dP/dQ_N)_{\max, \text{stage II}}$ , shows a robust linear correlation with modulus, enabling modulus evolution to be directly extracted from experimental pressure-capacity data. Importantly, deviations from this relationship provide mechanistic fingerprints of degradation: abnormal gas generation and excessive SEI growth reduce modulus, whereas lithium plating increases it. These insights establish a theoretical and experimental foundation for using pressure signals not only as indicators of SOH but also as diagnostic tools for identifying specific failure pathways. Although validated here on a limited set of LFP prismatic cells, the framework provides a new perspective for integrating mechanical signals into battery management systems. Future work should extend this approach across wider load conditions, diverse electrode chemistries, and complex failure scenarios, such as gas accumulation and packaging failure, to establish the modulus as a robust and generalizable indicator of battery mechanical degradation and failure. It is worth noting that although the pressure signal can serve as an indicator to describe the degradation state of the battery, there is still a lack of pressure sensors that can be effectively applied in actual battery modules. This is because it involves challenges such as the cost, size, integration difficulty, signal stability, and calibration drift of the sensors [47]. Only by simultaneously developing pressure analysis theory and pressure sensing technology can the industrial application value of current research be enhanced.

**Author Contributions:** Conceptualization, S.L. and X.-G.Y.; methodology, S.L. and X.L.; hardware setup, J.S. and X.F. (Xingcun Fan); validation, W.W.; formal analysis, Z.C.; investigation, X.F. (Xiaolong Feng); resources, X.L.; data curation, J.L. and H.L.; writing—original draft preparation, S.L.; writing—review and editing, X.-G.Y.; visualization, S.L.; supervision, J.J.; project administration, X.L.; funding acquisition, X.-G.Y. All authors have read and agreed to the published version of the manuscript.

**Funding:** This research was funded by National Natural Science Foundation of China (52277212), Shenzhen Science and Technology Program (KJZD20230923114611023), and the national program of China.

**Data Availability Statement:** The data that support the plots within this paper and other findings of this study are available from the corresponding author on reasonable request.

**Conflicts of Interest:** Author Xue Li, Jintao Shi, Xingcun Fan, Zifeng Cong and Xiaolong Feng were employed by the company China Automotive New Energy Technology Co., Ltd. The remaining authors declare that the research was conducted in the absence of any commercial or financial relationships that could be construed as a potential conflict of interest.

## Abbreviations

The following abbreviations are used in this manuscript:

LFP	Lithium Iron Phosphate
SOH	State of Health
SEI	Solid Electrolyte Interphase
LiB	Lithium-ion batterie
EES	Electrochemical Energy Storage
EV	Electric Vehicle
SOC	State of Charge
BMS	Battery Management System
LLI	Loss of Lithium Inventory
LAM	Loss of Active Material
RPT	Reference Performance Test
BOL	Beginning of Life

## Appendix A

Table A1 presents the previous research designs and our current research design, in order to illustrate the differences and innovations of this study compared to other studies. Our study uses larger-capacity prismatic batteries, exceeding the battery capacity range in previous studies; the analysis of pressure is more in-depth, and new data processing methods have been proposed; a lower preload force for cylindrical batteries has been set to study the pressure range that has not been explored; different temperatures have been adopted to study the influence of temperature on pressure when under pressure.

**Table A1.** Our research compared with previous studies.

Research	Object of Study	Mechanical Characteristics Under the Study	Preload	Temperature
Cannarella [14]	pouch cell (0.5 Ah)	reversible and irreversible components	50 kPa/500 kPa/5000 kPa	25 °C
Niu [33]	pouch cell (2.4 Ah)	irreversible component	50 kPa/200 kPa/500 kPa	25 °C
Ding [34]	pouch cell (2.5 Ah)	reversible component	70 kPa	25 °C
Wang [36]	prismatic cell (86 Ah)	reversible component; stress-strain curves	1 kN/2 kN/8 kN (43 kPA/87 kPA/348 kPA)	25 °C
Our research	prismatic cell (>150 Ah)	reversible and irreversible components; stress-strain curves; dP/dQ curve	25 kPa/50 kPa	25 °C/45 °C/55 °C

Table A2 provides the charging protocol for 1.6C-MCC. 1.6C refers to the average rate from 20% SOC to 80% SOC.

**Table A2.** 1.6C-MCC protocol.

Step	Operation
1	1C-CC for 360 s
2	2.3C-CC for 235 s
3	2.1C-CC for 85.7 s
4	1.9C-CC for 188.8 s
5	1.7C-CC for 211.5 s
6	1.5C-CC for 120 s
7	1.4C-CC for 128.5 s
8	1.2C-CC for 300 s
9	0.9C-CC for 400 s

10	0.8C-CC for 225 s
11	0.5C-CC to 3.8 V
12	CV to 0.05C

## Appendix B

Compression test information is shown in Figures A1 and A2 and Table A3. As shown in the Figure A2, except for the two experimental sample data of #cw which have significant differences, the experimental results of the other groups' two samples show little variation. This is because the injection volume of the dry cell affects the experimental results when the battery is initially compressed. In the main text, the representative curve is selected from the left side of each group's stress-strain curve.

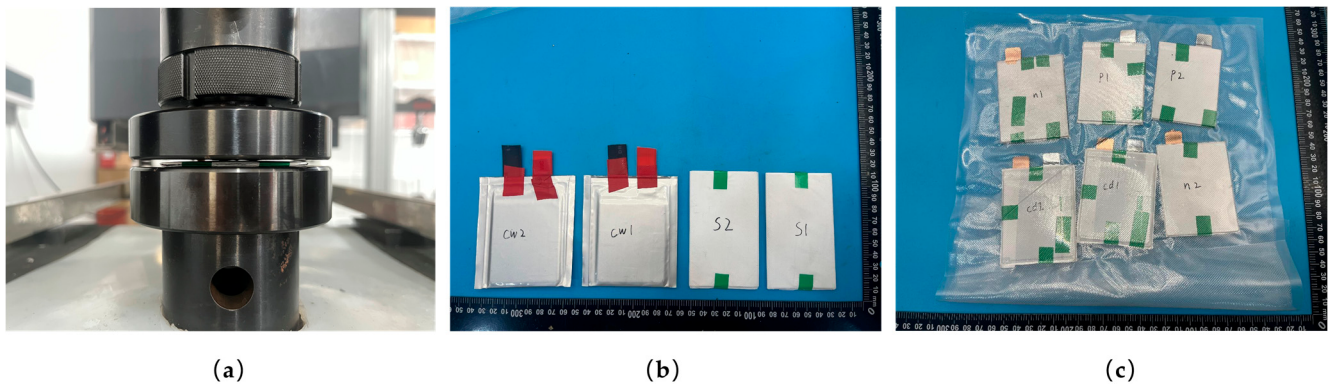


**Figure A1.** Compression test platform and samples (a) Photo of the extrusion platform (with samples placed in the platform); (b) Photo of samples: #cw and #s; (c) Photo of samples: #p, #n and #cd (The scale in the figure is in mm).

**Table A3.** Compression sample information.

Sample Name	Meaning of the Name	Size (Length × Width × Thickness)
#p	positive electrode (cathode)	74 mm * 57 mm * 1.5 mm
#n	negative electrode (anode)	77 mm * 60 mm * 1.5 mm
#s	separator	100 mm * 60 mm * 1.5 mm
#cd	cell-dey	80 mm * 62 mm * 3 mm
#cw	cell-wet	80 mm * 60 mm * 3 mm

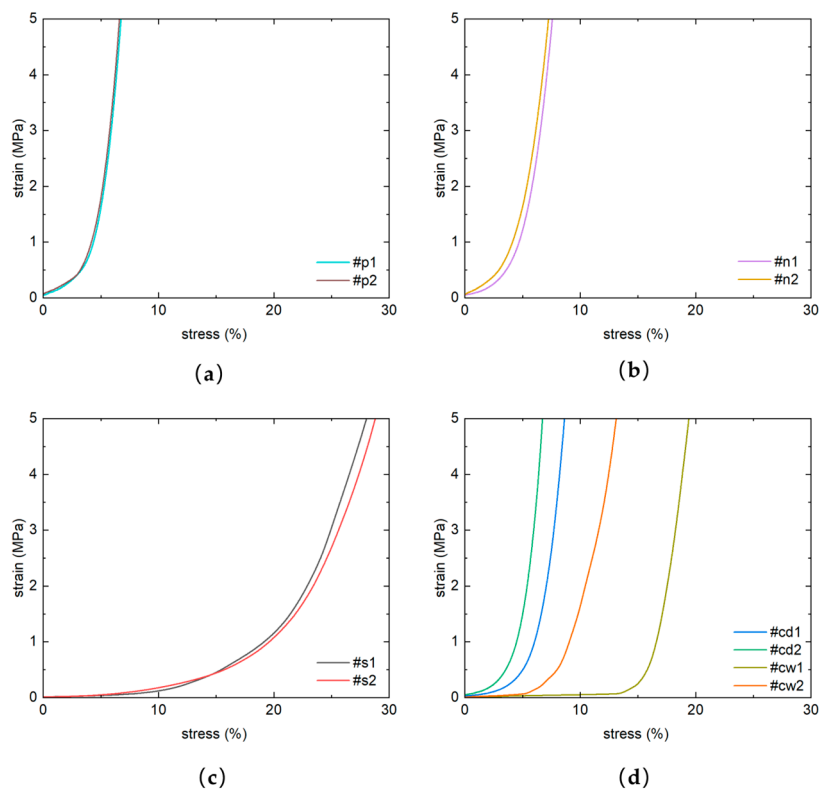


**Figure A2.** The stress–strain curves of the samples (a) #p1 and #p2; (b) #n1 and #n2; (c) #s1 and #s2; (d) #cd1, #cd2, #cw1 and #cw2.

## Appendix C

According to Figure 3b, the data points of the two samples at 25 °C–50 kPa and 45 °C–50 kPa are highly coincident around SOH = 96%/95%/93%, which indicates that the SOH and  $P_0$  corresponding to these data points are approximately the same, with only the temperature being different. These data points can be used for comparative analysis of the influence of thermal expansion and electrochemical side reactions on pressure. The corresponding pressures of these data points are shown in Figure A3. It can be seen from the figure that the pressure curves at the same SOH but different temperatures have good coincidence, while the pressure curves at the same temperature but different SOH have a large degree of dispersion. This suggests that compared with the promoting effect of electrochemical side reactions on pressure, the influence of thermal expansion on pressure is relatively small.

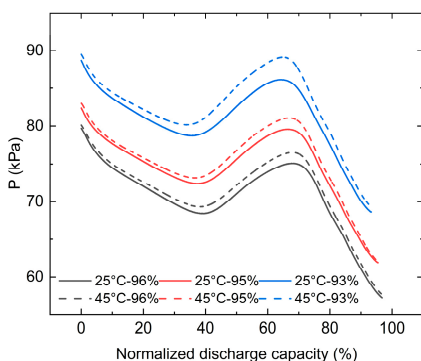


**Figure A3.** Comparison of pressure curves at different temperatures and SOH (with the same preload and the same  $P_0$ ).

## Appendix D

Typically, the conventional approach to obtain differential curves involves differentiating the raw data at the minimum sampling interval followed by subsequent smoothing. This is because raw data is often contaminated with noise, and the results obtained by direct differentiation at the minimum interval fail to reveal clear patterns, thus necessitating further smoothing. However, smoothing can obscure data features, and a relatively large smoothing window is required to eliminate noise, which further obscures the data features. As illustrated in Figure A4a,b, significant noise remains even with a smoothing window containing 60 sampling points.

To obtain high-quality  $dP/dQ_N-Q_N$  curves, the present study did not employ the “differentiating + smoothing” approach for processing the raw data. Instead, it adopted the method of gradually increasing the differentiation step size, as shown in Equation (A1):

$$\frac{dP}{dQ_N} = \frac{f(P_{right} - P_{left})}{(\Delta Q_N)_f} \quad (\text{A1})$$

where  $f$  is the differentiation step size,  $(\Delta Q_N)_f$  represents the normalized capacity corresponding to the step interval, and  $P_{right}$  and  $P_{left}$  denote the pressures at the right and left ends of this interval, respectively. For an interval also containing 60 sampling points, our method demonstrates superior noise-removal capability, as shown in Figure A4c.

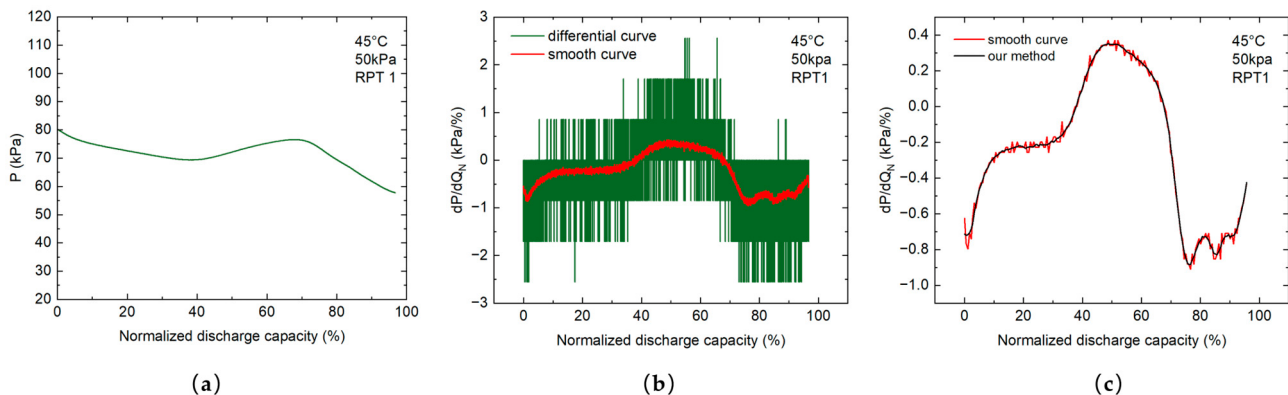


**Figure A4.** Take 45 °C–50kPa-RPT1 as an example to show the data processing effect: (a)  $P-Q_N$  curve; (b) differentiating with the minimum sampling interval and smoothing with a window of 60 sampling data; (c) comparison of the smoothed  $dP/dQ_N-Q_N$  curve and the  $dP/dQ_N-Q_N$  processed by our method.

## Appendix E

The RPT pressure data of the verification experiment are shown in Figure A5., with the experimental conditions being 60 °C and the initial load being 50 kPa.

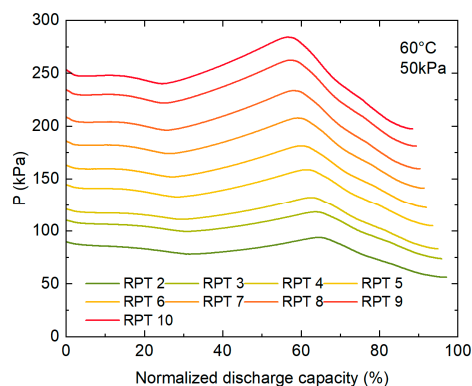


**Figure A5.** The RPT pressure data of the verification experiment.

## References

- Yang, X.G.; Liu, T.; Wang, C.Y. Thermally modulated lithium iron phosphate batteries for mass-market electric vehicles. *Nat. Energy* **2021**, *6*, 176–185.
- Li, Y.K.; Wei, C.; Sheng, Y.M.; Jiao, F.P.; Wu, K. Swelling Force in Lithium-Ion Power Batteries. *Ind. Eng. Chem. Res.* **2020**, *59*, 12313–12318.
- Schmitt, J.; Kraft, B.; Schmidt, J.P.; Meir, B.; Elian, K.; Ensling, D.; Keser, G.; Jossen, A. Measurement of gas pressure inside large-format prismatic lithium-ion cells during operation and cycle aging. *J. Power Sources* **2020**, *478*, 228661.
- Cai, T.; Valecha, P.; Tran, V.; Engle, B.; Stefanopoulou, A.; Siegel, J. Detection of Li-ion battery failure and venting with Carbon Dioxide sensors. *Etransportation* **2021**, *7*, 100100.
- Park, K.; Myeong, S.; Shin, D.; Cho, C.W.; Kim, S.C.; Song, T. Improved swelling behavior of Li ion batteries by microstructural engineering of anode. *J. Ind. Eng. Chem.* **2019**, *71*, 270–276.
- Choi, Y.H.; Lim, H.K.; Seo, J.H.; Shin, W.J.; Choi, J.H.; Park, J.H. Development of Standardized Battery Pack for Next-Generation PHEVs in Considering the Effect of External Pressure on Lithium-Ion Pouch Cells. *Sae Int. J. Altern. Powertrains* **2018**, *7*, 195–205.
- Mao, S.Y.; Han, X.B.; Lu, Y.; Wang, D.P.; Su, A.Y.; Lu, L.G.; Feng, X.N.; Ouyang, M.G. Multi sensor fusion methods for state of charge estimation of smart lithium-ion batteries. *J. Energy Storage* **2023**, *72*, 108736.
- Gu, X.B.; Wang, X.Y.; Ren, Y.; Zhou, W.Q.; Huan, X.; Siegel, J.; Jiang, W.R.; Song, Z.Y. Mechanical information enhanced battery state-of-health estimation. *Etransportation* **2025**, *25*, 100440.
- Xu, Q.; Wang, X.Y.; Ye, H.; Gong, L.L.; Tan, P.; Pan, T.R. An accurate state of health estimation method for lithium-ion batteries based on expansion force analysis. *Energy* **2025**, *325*, 136155.
- Choi, H.; Son, H.; Choi, Y.H.; Youn, B.D.; Lee, G. Reliability-based design optimization of a pouch battery module using Gaussian process modeling in the presence of cell swelling. *Struct. Multidiscip. Optim.* **2023**, *66*, 227.
- Yuan, C.H.; Hahn, Y.; Lu, W.Q.; Oancea, V.; Xu, J. Quantification of electrochemical-mechanical coupling in lithium-ion batteries. *Cell Rep. Phys. Sci.* **2022**, *3*, 101158.
- Müller, V.; Scurtu, R.G.; Memm, M.; Danzer, M.A.; Wohlfahrt-Mehrens, M. Study of the influence of mechanical pressure on the performance and aging of Lithium-ion battery cells. *J. Power Sources* **2019**, *440*, 227148.
- Chen, K.X.; Xu, Y.H.; Wu, H.; Zhu, J.G.; Wang, X.Y.; Chen, S.Q.; Wei, X.Z.; Dai, H.F. Degradation mechanism and assessment for different cathode based commercial pouch cells under different pressure boundary conditions. *Energy Storage Mater.* **2024**, *73*, 103793.
- Cannarella, J.; Arnold, C.B. Stress evolution and capacity fade in constrained lithium-ion pouch cells. *J. Power Sources* **2014**, *245*, 745–751.
- Du, X.N.; Hu, Y.; Choe, S.Y.; Garrick, T.R.; Fernandez, M.A. Characterization and analysis of the effect of pressure on the performance of a large format NMC/C lithium-ion battery. *J. Power Sources* **2023**, *573*, 233117.
- Aufschläger, A.; Durdel, A.; Kraft, L.; Jossen, A. Optimizing mechanical compression for cycle life and irreversible swelling of high energy and high power lithium-ion pouch cells. *J. Energy Storage* **2024**, *76*, 109883.
- Wünsch, M.; Kaufman, J.; Sauer, D.U. Investigation of the influence of different bracing of automotive pouch cells on cyclic lifetime and impedance spectra. *J. Energy Storage* **2019**, *21*, 149–155.

18. Cannarella, J.; Arnold, C.B. Ion transport restriction in mechanically strained separator membranes. *J. Power Sources* **2013**, *226*, 149–155.
19. Sauerteig, D.; Hanselmann, N.; Arzberger, A.; Reinshagen, H.; Ivanov, S.; Bund, A. Electrochemical-mechanical coupled modeling and parameterization of swelling and ionic transport in lithium-ion batteries. *J. Power Sources* **2018**, *378*, 235–247.
20. Müller, V.; Scurtu, R.G.; Richter, K.; Waldmann, T.; Memm, M.; Danzer, M.A.; Wohlfahrt-Mehrens, M. Effects of Mechanical Compression on the Aging and the Expansion Behavior of Si/C-Composite|NMC811 in Different Lithium-Ion Battery Cell Formats. *J. Electrochem. Soc.* **2019**, *166*, A3796–A3805.
21. Aufschläger, A.; Kücher, S.; Kraft, L.; Spingler, F.; Niehoff, P.; Jossen, A. High precision measurement of reversible swelling and electrochemical performance of flexibly compressed 5 Ah NMC622/graphite lithium-ion pouch cells. *J. Energy Storage* **2023**, *59*, 106483.
22. Deich, T.; Storch, M.; Steiner, K.; Bund, A. Effects of module stiffness and initial compression on lithium-ion cell aging. *J. Power Sources* **2021**, *506*, 230163.
23. Koo, J.K.; Yun, Y.; Seo, J.K.; Ha, S.H.; Kim, D.W.; Mun, J.; Kim, Y.J. Detrimental electrochemical behavior caused by excessive high pressure on Li-ion pouch-type full cell. *Electrochim. Commun.* **2023**, *152*, 107518.
24. Hahn, S.; Theil, S.; Kroggel, J.; Birke, K.P. Pressure Prediction Modeling and Validation for Lithium-Ion Pouch Cells in Buffered Module Assemblies. *J. Energy Storage* **2021**, *40*, 102517.
25. Rieger, B.; Schlueter, S.; Erhard, S.V.; Schmalz, J.; Reinhart, G.; Jossen, A. Multi-scale investigation of thickness changes in a commercial pouch type lithium-ion battery. *J. Energy Storage* **2016**, *6*, 213–221.
26. Wu, B.; Lu, W. A battery model that fully couples mechanics and electrochemistry at both particle and electrode levels by incorporation of particle interaction. *J. Power Sources* **2017**, *360*, 360–372.
27. Yang, K.; Zhang, W.K.; Yin, Y.; Nan, J.R.; Wang, W.W.; Jiang, J.C.; Yang, X.G. A hierarchical electrochemical-thermal-mechanical coupled model capable of predicting non-uniform behaviors in large-format Li-ion cells. *J. Power Sources* **2025**, *629*, 236049.
28. Louli, A.J.; Ellis, L.D.; Dahn, J.R. Operando Pressure Measurements Reveal Solid Electrolyte Interphase Growth to Rank Li-Ion Cell Performance. *Joule* **2019**, *3*, 745–761.
29. Huang, W.X.; Ye, Y.S.; Chen, H.; Vilá, R.A.; Xiang, A.; Wang, H.X.; Liu, F.; Yu, Z.A.; Xu, J.W.; Zhang, Z.W.; et al. Onboard early detection and mitigation of lithium plating in fast-charging batteries. *Nat. Commun.* **2022**, *13*, 7091.
30. Wang, S.; Ren, D.S.; Xu, C.S.; Han, X.B.; Liu, X.; Lu, L.G.; Ouyang, M.G. Lithium plating induced volume expansion overshoot of lithium-ion batteries: Experimental analysis and modeling. *J. Power Sources* **2024**, *593*, 233946.
31. Ge, X.Y.; Zhang, Y.; Du, R.; Chen, N.; Yu, Y.F.; Li, Z.; Huang, Y.H. Revealing the electrochemical-mechanical correspondence between electrode films and 20 Ah prismatic Li-ion batteries via optical fiber monitoring. *Chem. Eng. J.* **2024**, *488*, 150895.
32. Li, R.; Ren, D.; Guo, D.; Xu, C.; Fan, X.; Hou, Z.; Lu, L.; Feng, X.; Han, X.; Ouyang, M. Volume deformation of large-format lithium ion batteries under different degradation paths. *J. Electrochem. Soc.* **2019**, *166*, A4106.
33. Niu, Z.C.; Sun, Z.W.; Zhang, S.; Xia, Y. Model development for predicting irreversible swelling of aged lithium iron phosphate/graphite pouch cells under different pressures and temperatures. *J. Power Sources* **2025**, *641*, 236884.
34. Ding, S.C.; Wang, L.; Dai, H.F.; He, X.M. Prognosticating nonlinear degradation in lithium-ion batteries: Operando pressure as an early indicator preceding other signals of capacity fade and safety risks. *Energy Storage Mater.* **2025**, *75*, 103998.
35. Cao, Y.Z.; Wang, H.C.; Liu, B.H.; Xu, J. Modeling, validation, and analysis of swelling behaviors of lithium-ion batteries. *J. Energy Storage* **2023**, *74*, 109499.
36. Wang, H.C.; Wu, Y.B.; Cao, Y.Z.; Liu, M.T.; Liu, X.; Liu, Y.; Liu, B.H. Investigate the changes of aged lithium iron phosphate batteries from a mechanical perspective. *Iscience* **2024**, *27*, 111300.
37. Zhang, C.; Xu, J.; Cao, L.; Wu, Z.N.; Santhanagopalan, S. Constitutive behavior and progressive mechanical failure of electrodes in lithium-ion batteries. *J. Power Sources* **2017**, *357*, 126–137.
38. Weng, A.D.; Olide, E.; Kovalchuk, I.; Siegel, J.B.; Stefanopoulou, A. Modeling Battery Formation: Boosted SEI Growth, Multi-Species Reactions, and Irreversible Expansion. *J. Electrochem. Soc.* **2023**, *170*, 090523.
39. von Kolzenberg, L.; Latz, A.; Horstmann, B. Chemo-Mechanical Model of SEI Growth on Silicon Electrode Particles. *Batter. Supercaps* **2022**, *5*, e202100216.
40. Cao, Y.Z.; Wang, H.C.; Liu, B.H. Multi-scale swelling behaviors and mechanisms of graphite electrode-based lithium-ion battery at various charging rates. *J. Power Sources* **2024**, *606*, 234504.
41. Mohtat, P.; Lee, S.; Siegel, J.B.; Stefanopoulou, A.G. Towards better estimability of electrode-specific state of health: Decoding the cell expansion. *J. Power Sources* **2019**, *427*, 101–111.

42. Clerici, D.; Mocera, F.; Soma, A. Electrochemical-mechanical multi-scale model and validation with thickness change measurements in prismatic lithium-ion batteries. *J. Power Sources* **2022**, *542*, 231735.
43. Winter, M.; Besenhard, J.O.; Spahr, M.E.; Novak, P. Insertion Electrode Materials for Rechargeable Lithium Batteries. *Adv. Mater.* **1998**, *10*, 725–763.
44. Yang, X.G.; Leng, Y.J.; Zhang, G.S.; Ge, S.H.; Wang, C.Y. Modeling of lithium plating induced aging of lithium-ion batteries: Transition from linear to nonlinear aging. *J. Power Sources* **2017**, *360*, 28–40.
45. Hosseinzadeh, E.; Marco, J.; Jennings, P. The impact of multi-layered porosity distribution on the performance of a lithium ion battery. *Appl. Math. Model.* **2018**, *61*, 107–123.
46. Li, N.; Chen, H.; Zhang, X.M.; Han, J.Q.; Wang, J.; Wang, X.M. Simultaneous prediction of rock matrix modulus and critical porosity. *Appl. Geophys.* **2019**, *16*, 14–24.
47. Wang, W.; Liu, S.; Ma, X.-Y.; Jiang, J.; Yang, X.-G., Advancing Smart Lithium-Ion Batteries: A Review on Multi-Physical Sensing Technologies for Lithium-Ion Batteries. *Energies* **2024**, *17*, (10), 2273.

**Disclaimer/Publisher’s Note:** The statements, opinions and data contained in all publications are solely those of the individual author(s) and contributor(s) and not of MDPI and/or the editor(s). MDPI and/or the editor(s) disclaim responsibility for any injury to people or property resulting from any ideas, methods, instructions or products referred to in the content.